ACS NANO

www.acsnano.org

ARTICLE

Spin-Polarized Photoemission from Chiral CuO Catalyst Thin Films

Paul V. Möllers,* Jimeng Wei, Soma Salamon, Manfred Bartsch, Heiko Wende, David H. Waldeck, and Helmut Zacharias*

Cite This: *ACS Nano* 2022, 16, 12145–12155

Read Online

ACCESS | Metrics & More | Article Recommendations | Supporting Information

ABSTRACT: **The chirality-induced spin selectivity (CISS) effect facilitates a paradigm shift for controlling the outcome and efficiency of spin-dependent chemical reactions, for example, photoinduced water splitting. While the phenomenon is established in organic chiral molecules, its emergence in chiral but inorganic, nonmolecular materials is not yet understood. Nevertheless, inorganic spin-filtering materials offer favorable characteristics, such as thermal and chemical stability, over organic, molecular spin filters. Chiral cupric oxide (CuO) thin films can spin polarize (photo)electron currents, and this capability is linked to the occurrence of the CISS effect. In the present work, chiral CuO films, electrochemically deposited on partially UV-transparent polycrystalline gold substrates, were subjected to deep-UV laser pulses, and the average spin polarization of photoelectrons was measured in a Mott scattering apparatus. By energy resolving the photoelectrons and changing the photoexcitation geometry, the energy distribution and spin polarization of the photoelectrons originating from the Au substrate could be distinguished from those arising from the CuO film. The findings reveal that the spin polarization is energy dependent and, furthermore, indicate that the measured polarization values can be rationalized as a sum of an intrinsic spin polarization in the chiral oxide layer and a contribution via CISS-related spin filtering of electrons from the Au substrate. The results support efforts toward a rational design of further spin-selective catalytic oxide materials.**

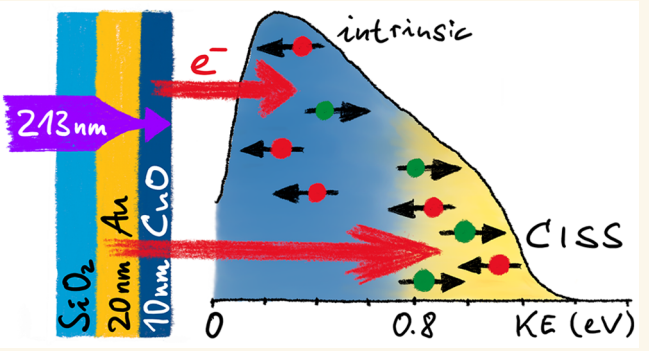

KEYWORDS: *CISS, cupric oxide, catalysis, chirality, electron spin, Mott scattering*

The electrolysis of water holds promise to provide a route for the production of hydrogen, which is a sustainable fuel when generated by electricity from renewable energy sources, like wind power, photovoltaics, or direct water splitting by sunlight.[1−4] For the latter process, the overall efficiency of the water-splitting reaction, comprising the hydrogen evolution reaction (HER) at the cathode and the oxygen evolution reaction (OER) at the anode, is severely limited by the high overpotential required for the OER.[5] Because molecular oxygen is a triplet species in its ground state, the overpotential is thought to arise partially from spin constraints in the formation of the O═O double bond. Furthermore, the OER at the anode suffers from side reactions, such as the generation of hydrogen peroxide, which can degrade the electrode material.

Recent work has demonstrated that the electron spin provides a means to control and enhance the chemical selectivity of the electrocatalytic water-splitting reaction.[6−10] The OER involves the transfer of four electrons to the anode, that is, through the catalytic surface of the electrode material, and the generation of surface-adsorbed radical intermediates (OH, O, OOH). If the electron current to the anode is spin polarized, then so must be the intermediate radicals generated on the catalyst surface. The spin polarization is believed to favor the formation of triplet oxygen and to suppress the generation of singlet byproducts, such as hydrogen peroxide. The initial implementations[6−8] of this concept were based on the chirality-induced spin selectivity (CISS) effect[11] in chiral organic molecule layers that were adsorbed on the electrode surface. This concept was extended to intrinsically chiral cupric oxide (CuO)[9] and cobalt oxide (CoO_x)[10] catalyst materials, which spin filter electron currents and therefore spin polarize

Received: March 18, 2022
Accepted: July 18, 2022
Published: August 9, 2022

https://doi.org/10.1021/acsnano.2c02709
ACS Nano 2022, 16, 12145−12155

intermediate radical species. While these explorative approaches have proven successful, the origin of the electron spin polarization in the chiral oxide layers is not yet understood. Direct electron polarimetry established CISS so far for helical organic molecules such as DNA,[12,13] PNA,[14] oligopeptides,[15] and helicene.[16] To promote the well-targeted improvement of these catalyst systems, an understanding of the spin-polarizing mechanism in the chiral oxide layers is required. This work explores the electron spin selectivity by spin-resolved photoemission measurements conducted with chiral CuO thin films that were electrochemically deposited onto 20 nm thick Au films using a method pioneered by Switzer et al.[17−19] Circular dichroism (CD) spectroscopy is used to confirm that the electrodeposited oxide films possess a well-defined chirality, and Mott polarimetry is used to quantify the spin-polarized photoelectron distributions. Photoelectrons are generated by UV laser radiation impinging either from the CuO-coated front or from the substrate (back) side of the UV-transparent samples. The photoelectron spectra indicate that the relative numbers of photoelectrons emitted from the CuO film itself and from the gold substrate depend on the illumination direction. It is found that, upon changing the excitation direction, which changes the source of photoelectrons from either the gold substrate or the chiral CuO film, the sign of the spin polarization changes. The results provide further evidence that the spin polarization in the chiral CuO layer is strongly energy dependent, because backside illumination yields electrons with higher kinetic energies. Magnetization curves indicate a weak ferromagnetic behavior in the chiral oxide layers and therefore suggest that the measured spin polarization could arise as a sum of the CISS effect and an intrinsic spin polarization in these layers due to structurally no longer compensated spins in the usually antiferromagnetically (AF) ordered CuO or by the Dzyaloshinsky-Moriya interaction.[20,21]

RESULTS AND DISCUSSION

Film Deposition and Characterization. While transition metal oxides are generally achiral, chiral oxide layers can be grown by the introduction of a chiral bias in the layer deposition process. Switzer et al. demonstrated the electrodeposition of chiral copper oxide layers from Cu(II)-ligand complexes in solution.[17,18] The films grown based on this method exhibit a well-defined oxidation state and crystallographic texture on both monocrystalline[17,18] and polycrystalline[17,19] substrates. Copper complexes with chiral ligands, such as tartaric acid, can be employed as chiral precursors to electrodeposit chiral CuO films.[18,22] The sense of the oxide film's chirality ("left" vs "right") is determined by the enantiomeric form of the ligand, and this enantioselectivity allows for the generation of films with identical chemical composition but opposite handedness.

For the present study, CuO films were electrodeposited from a solution containing chiral Cu(II)-tartrate complexes as described previously.[9] The film thickness as a function of the electrodeposition time was calibrated by atomic force microscopy (AFM) line profile measurements. Films with a thickness ranging from 5 to 40 nm were investigated. The films were deposited on fused silica slides coated with 20 nm thin gold films on 3 nm thin titanium adhesion layers. This allows for UV illumination from both the front (CuO) and back (substrate) side of the samples and for the acquisition of optical absorption and circular dichroism spectra. Samples with CuO layers deposited from complexes containing L-[(R,R)-(+)-] and D-[(S,S)-(−)-] tartaric acid are labeled as L- and D-CuO in the following.

The nanometer- to micrometer-scale film quality was evaluated by AFM measurements. Representative topography images are shown in section S1 of the Supporting Information. Consistent with previous scanning electron microscopy (SEM) studies,[9] the films have a crystalline structure. The crystallite size is comparable to the layer thickness, which gives rise to a rather high roughness of ∼10 nm at the nanometer scale. The topography is independent of the film's chirality. On the micrometer scale, the films are mostly continuous but, nevertheless, exhibit defects and inhomogeneities.

Copper Oxidation State. X-ray photoelectron spectroscopy (XPS) of the Cu 2p peak region allows one to determine the oxidation state of Cu in the film. A representative example is given in Figure 1. The chemical shift of the Cu $2p_{3/2}$ peak at

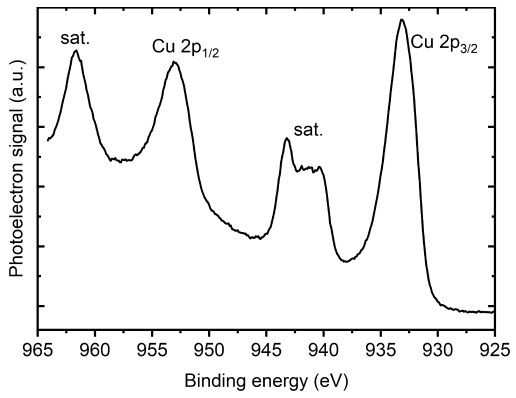

Figure 1. An XPS spectrum of the Cu 2p peak region, acquired on a 40 nm oxide thin film, is shown. At binding energies of 940−945 eV and at 963 eV two satellite peaks to the Cu $2p_{3/2}$ and $2p_{1/2}$ peaks, respectively, appear, which are indicative of CuO and absent for Cu_2O.[24]

E_b = 933 eV differs between CuO (i.e., Cu^{2+}) and Cu_2O (Cu^+) by ∼1.5 eV.[23] Multiplet broadening is only observed in the case of CuO, and the satellite peaks around $E_b \approx$ 940 to 945 and 963 eV, arising from shakeups of the $3d^9$ state of Cu^{2+}, are not present in Cu_2O.[24] Therefore, the observed spectra can unambiguously be assigned to originate from CuO. Survey spectra can be found in section S2 of the Supporting Information. Further high-resolution XPS spectra obtained from several oxide films were acquired in order to analyze for possible ferromagnetic contaminations from cobalt, iron, nickel, chromium, or manganese. Using both XPS and time-of-flight secondary ion mass spectroscopy (ToF-SIMS), no evidence of ferromagnetic contamination was found (see the Supporting Information, sections S2 and S3, for more detail). Further, no carbon residues from the organic seed precursor were detected in the film with either method after the preparation was finished by final heating.

Film Chirality. While the film deposition method employed here was unambiguously shown to generate chiral oxide films, the nature of this chirality is the subject of ongoing research. The means through which surfaces of materials with an achiral bulk structure (e.g., face-centered cubic (fcc) and body-centered cubic (bcc) lattices) can be rendered chiral were previously presented by Gellman.[25] Notably, surfaces of these materials with higher Miller indices (*hkl*) with $h \neq k$, $k \neq$

https://doi.org/10.1021/acsnano.2c02709
ACS Nano 2022, 16, 12145−12155

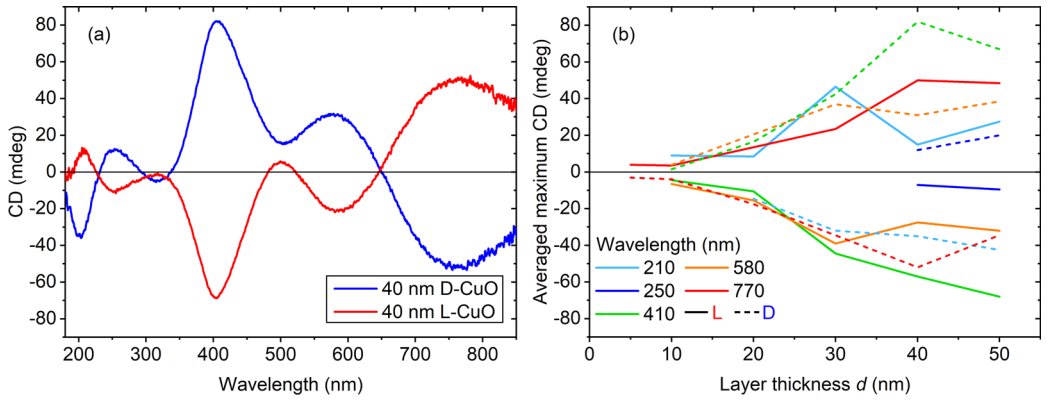

Figure 2. CD spectra measured on 40 nm CuO thin films of either handedness (a) and the CD magnitude at different wavelengths as a function of the film thickness (b).

l, $l \neq h$, and $h \times k \times l \neq 0$ can exhibit step edges with low symmetry that make the surfaces intrinsically chiral.[26] CuO has a monoclinic structure; that is, exactly one angle between the lattice vectors deviates from 90° and induces a screw symmetry along the b-axis [010]. Planes that are parallel to this axis are achiral, and those with $k \neq 0$ are chiral.[27] The chirality of the CuO layers is, besides optical CD measurements, predominantly established through X-ray diffraction (XRD)[18,22] and X-ray photoelectron diffraction (XPD)[22] measurements. These studies showed that the chiral CuO films have textures in which chiral planes are preferentially exposed along the sample surface plane. More specifically, the oxygen atoms in the CuO lattice structure can occupy two nonequivalent positions.[22] The XPD measurements, which are sensitive only to the topmost surface layers, reveal that the surface chirality is determined by which of these oxygen atoms terminate the surface. Switzer et al. also demonstrated that the chiral films can act as enantioselective catalysts.[17] Recent transmission electron microscopy (TEM) studies of similar compounds by Bai et al. furthermore indicate that the bulk crystal structure of the investigated nickel and iron oxide films is chirally distorted.[28,29]

To confirm that the films investigated in this study are chiral as expected, transmission circular dichroism (CD) spectra were acquired from each sample prior to the photoemission measurements. Figure 2a shows representative CD spectra measured on 40 nm CuO thin films of both L and D chirality. The spectra show a CD of up to 80 mdeg and confirm that the films are indeed chiral. The CD spectra of the L and D films are, to a good approximation, mirror images of one another, indicating that the films deposited from complexes with L- and D-tartaric acid have opposite chirality. The CD magnitudes at the various peak wavelengths are shown in Figure 2b as a function of the film thickness. A systematic increase of the CD magnitude with the film thickness is observed, which suggests that the chirality is retained throughout the entire layer thickness. This supports the notion of a chiral bulk structure, that is, a chirally distorted atomic lattice. The energetic positions of the spectral peaks (Figure 2a) do not shift with the film thickness.

Electronic Structure. Despite its relevance for high-temperature superconductivity, the electronic structure of CuO, in contrast to Cu_2O, is still not fully elucidated. Theoretical band structure calculations deviate more strongly from experimentally obtained results for CuO than is the case for Cu_2O, and this may result from strong electron−electron correlation effects near the valence band edge (VBE).[30,31] For very thin films, additional deviations from the bulk structure are possible, for example, due to (quantum) confinement effects or depending on a local film texture.

For initial characterization, baseline-corrected absorption spectra in the UV−vis−IR region were acquired. The data can be found in section S4 of the Supporting Information. At λ = 213 nm, the absorption coefficient is $\alpha = 3 \times 10^5$ cm^{-1}, corresponding to a 1/e penetration depth of ∼30 nm. Figure S6b,c shows Tauc plots that indicate the position of the main absorption edges. The direct and indirect band gaps are identified at ΔE_{dir} = 3.08 eV and ΔE_{ind} = 1.20 eV, respectively. The nature of the low-energy band gap is still under debate.[32] The higher-energy edge matches the position of the main peaks at λ = 410 nm in the CD spectra. The electronic structure of the samples was further characterized by He I ultraviolet photoelectron spectroscopy (UPS) measurements[33] of both a 200 nm CuO thin film and the bare gold substrate. An energy level diagram derived from these data is shown in Figure 3. The work function of the 20 nm gold substrate is determined to be Φ_{Au} = 4.65 eV. This value is reduced compared to the work function of bulk gold because of the low film thickness, consistent with literature values.[34] The work function of the CuO sample is determined to be Φ_{CuO} = 4.61 eV, and the VBE of CuO is located 0.34 eV below the Fermi

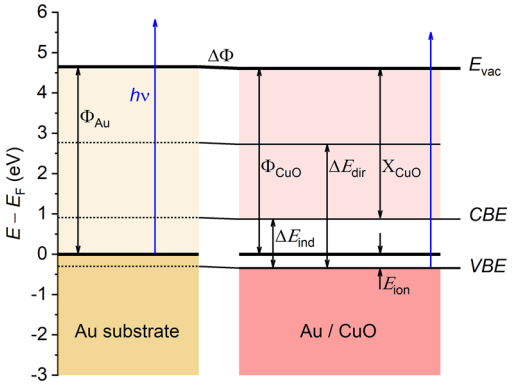

Figure 3. Energy scheme of the Au/CuO samples, determined from He I photoelectron spectra of a 200 nm CuO sample, and a bare gold substrate. Note that X_{CuO} is the electron affinity of CuO and that E_{ion} is the position of the valence band edge relative to the Fermi level E_F. A very slight shift $\Delta\Phi$ of the vacuum level is measured. The other energies are specified in the text.

https://doi.org/10.1021/acsnano.2c02709
ACS Nano 2022, 16, 12145−12155

level; that is, VBE = Φ_{CuO} + E_{ion} ≈ 4.95 eV. Indeed, copper vacancies make cupric oxide an intrinsic p-type semiconductor.[35] The VBE position is higher than in bulk samples, where VBE = 5.4 eV,[36] but consistent with reports for CuO thin films.[25] Similar values were obtained from UPS spectra of 30 nm thin CuO films.

Spin Polarization Measurements. The spin polarization of photoelectrons emitted from the samples was measured in a Mott scattering apparatus, illustrated in Figure 4a, and described previously.[9] Photoelectrons are excited by laser pulses at λ = 213 nm ($h\nu$ = 5.83 eV) with a pulse duration of 200 ps and at a repetition rate of 20 kHz. The light impinges on the samples along the surface normal, perpendicular to the surface plane, and the photoelectrons are as well collected along the surface normal. In the experimental geometry used, the spin polarization along the surface normal of the samples is measured. Throughout the measurement procedure, the polarization of the laser light is interchanged from s-linear to clockwise (cw) and counterclockwise (ccw) circular by the rotation of a quarter-wave plate (QWP). At each position of the QWP, about 10^4 electrons are collected. After a full QWP rotation, the measurement position is interchanged between the sample and a polycrystalline gold substrate without an oxide layer, mounted directly beneath the sample. The polycrystalline gold emits unpolarized electrons upon excitation with linearly polarized light and is used to correct for instrumental asymmetries.

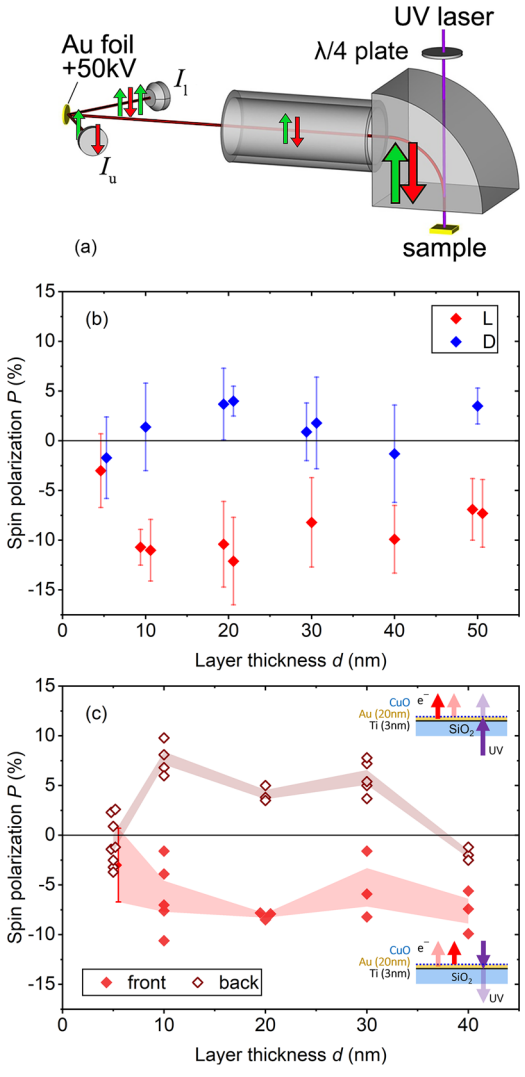

Figure 4. (a) Simplified scheme of the Mott scattering setup. (b) Spin polarization measured upon front side excitation with linearly polarized light for L- and D-CuO films.[9] (c) Further, technically identical measurements (full symbols) and measurements with the laser impinging on the back side of the partially UV-transparent samples (empty symbols). Note that the plots in (b, c) have different scales for their horizontal axes. The red-shaded areas indicate the standard deviation $\sigma/\sqrt{n}$, normalized to the number n of individual measurements. In Figure 4c, only one data point is available for 5 nm thin films; here, the uncertainty of the single measurement is indicated. Figure 4b reprinted with permission from ref 9. Copyright 2019 American Chemical Society.

In Figure 4b, the results from our previously published spin-resolved photoemission study[9] on chiral CuO layers are shown, where the illumination occurred from the front (CuO) side of the sample. Each data point comprises ∼100 single measurements, that is, ∼10^6 measured electrons. From samples coated with 5−50 nm thin CuO films, photoelectrons with an average spin polarization of up to P = −10 to −12% are emitted upon excitation with linearly polarized laser pulses at λ = 213 nm. These values were obtained from L-CuO films. The negative sign corresponds to electrons whose spin is aligned antiparallel to the electron momentum, that is, antiparallel to the surface normal of the sample. The values measured on D-CuO layers, that is, on layers with opposite chirality, on average show a spin polarization with the opposite sign of polarization, albeit at less significant values. The smaller magnitude of the spin polarization in these samples is the subject of further investigations, and we focus on the L-CuO samples in this study. However, the correct calibration of the Mott polarimeter was carefully confirmed prior and subsequent to each individual spin polarization measurement. The data include many samples, and L and D samples were measured in random order. Thus, a systematic error in the spin polarization toward negative values seems to be unlikely. This asymmetry of the spin polarization values is therefore a property of the chiral CuO films. In Figure 4c, results of additional spin polarization measurements on 5−40 nm thick L-CuO layers are shown. Filled diamond symbols correspond to measurements in which the sample was irradiated from the CuO-coated front side in technically identical measurements as shown in Figure 4b. Multiple data points at each thickness correspond to spin polarization measurements on different positions of the sample surface. With an uncertainty $\Delta P = \sigma/\sqrt{n}$ of up to $\Delta P = \pm$ 1.9% points, the standard deviation σ normalized to the number of measurements n, shown in the shaded area, reveals a considerable spread of the results on most samples. We previously considered only the maximum values on each sample, as reduced values are most likely due to inhomogeneities and defects on the surface and hence do not reflect the true spin polarization capacity of the samples. The spin polarization values shown in Figure 4b,c are consistent with one another.

Further measurements were conducted with the laser impinging on the back side of the sample, as illustrated in the inset of Figure 4c, and the results of these measurements are shown as open diamond symbols. We note that the same samples and the same surface areas were studied as for front side illumination, within the positioning accuracy of the 300 μm diameter of the laser beam. Because the substrate is UV-transparent fused silica, most (∼80%) of the light is absorbed

https://doi.org/10.1021/acsnano.2c02709
ACS Nano 2022, 16, 12145−12155

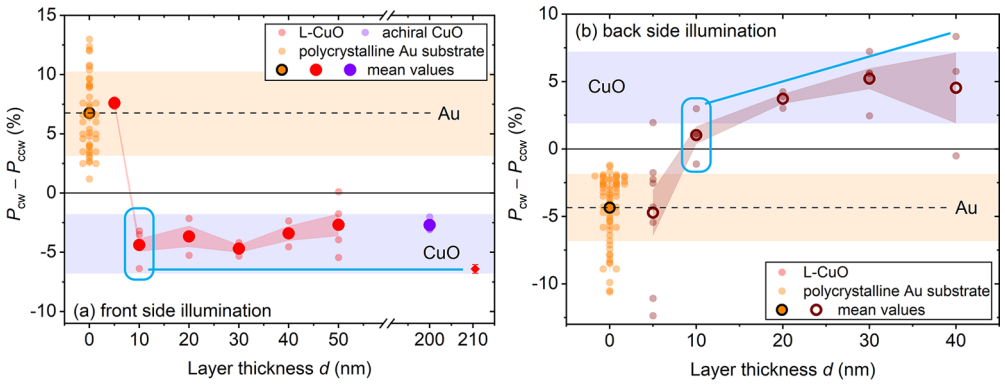

Figure 5. Differential spin polarization measured upon excitation with cw and ccw circularly polarized light impinging on either the front (a) or back (b) side of the samples. The standard deviation $\sigma/\sqrt{n}$, normalized to the number n of individual measurements, is indicated by the red-shaded area. The light blue lines are a guide; overlapping points are offset for clarity. The same sample areas were studied in (a, b).

in the gold layer underneath the CuO films. Further, the CuO film thickness is in the range of the electron mean free path (MFP). Hence the relative amount of the photoelectrons originating in the gold layer, instead of the CuO film, is expected to be significantly increased for these measurements as compared to front side illumination. As with front side illumination, no significant spin polarization is obtained from the 5 nm thin CuO films, and the highest polarization of $P \approx +10\%$ is obtained from the 10 nm thick films. Notably, the sign of the spin polarization is positive upon irradiation from the back side; that is, the electrons spins are, on average, aligned parallel to the electron momentum, in contrast to the illumination from the front side. For the 40 nm thick film, however, a negative polarization is measured independently of the direction of illumination. To understand these results, the origin of the photoelectrons excited from both the front and back sides of the samples is discussed in the following.

Origin of the Photoelectrons. The inelastic MFP of electrons traveling through the nonmolecular solid follows a general empirical dependency on the electron energy.[37] This dependency reflects the energy-dependent cross sections of different excitation processes, such as the generation of phonons, plasmons, or electron−hole pairs. On the basis of the work function of the CuO samples and the employed laser photon energy, the electrons that are measured in the present work have energies of $E - E_F \approx 4.6-5.8$ eV with respect to the Fermi level. The MFP at these energies is in the range of 4−8 nm, on the order of the film thickness. Hence, a careful analysis of the electron's origin for the different measurements is conducted below.

Intrinsic Spin Polarization. In materials with significant intrinsic spin−orbit coupling, the spin degeneracies in the valence band are lifted, and electrons can be excited into specific final spin states. In the present experimental geometry both light irradiation and electron emission occur along the surface normal. In this highly symmetric configuration and with centrosymmetric surfaces, such as the (111) surface of metals with an fcc crystal lattice (e.g., gold), unpolarized electrons are emitted upon irradiation with unpolarized or linearly polarized light. Circularly or elliptically polarized light excites spin-polarized electrons,[38−40] and the sign of the spin polarization is reversed due to symmetry constraints if the direction of the photon's circular polarization, clockwise or counterclockwise, is reversed, that is, $P_{cw} = -P_{ccw}$. As a manifestation of the spin-split band structure of the material, this spin polarization is material specific. Because the polarization of the incident laser light was interchanged between s-linear, cw, and ccw circular throughout the spin polarization measurement procedure, these data provide the initial evidence that irradiation of the samples from the front side predominately generates photoelectrons from the CuO film rather than from the gold substrate underneath it.

Figure 5a shows the spin polarization difference $(P_{cw} - P_{ccw})$ upon excitation with circularly polarized light impinging on the front side of the samples. The data points at $d = 0$ nm (orange) are measured on a bare polycrystalline gold substrate, from which an average differential polarization of $(P_{cw} - P_{ccw}) \approx (6.8 \pm 0.5)\%$ is observed in this excitation geometry. The deviations of the single measurements from the mean value reflect variations in the local crystallinity of the surface. At the other extreme of the thickness range, on 200 and 210 nm thick CuO films, the electron MFP of 4−8 nm and the light penetration depth of ∼30 nm in CuO imply that all of the detected photoelectrons originate from the CuO layer. These samples are therefore used as a CuO reference. On these samples, a differential polarization of $(P_{cw} - P_{ccw}) \approx -3\%$ is measured upon excitation from the front side.

For 5 nm thin CuO films the polarization values are mostly comparable to the values measured at the bare Au substrate, which suggests that the electrons are mostly excited in the gold layer. For a film thickness of $d = 10$ nm and larger, the spin polarization values consistently and significantly deviate from what is measured on gold and closely resemble the polarization measured on the CuO reference samples. The broader distribution of the individual results suggests that the layers are laterally inhomogeneous over the sample surface area. The average photoelectron spin polarization, however, does not change with the CuO film thickness. Thus, for CuO films with a thickness of 10 nm or more, the detected photoelectrons originate predominantly from the oxide film rather than from the gold substrate, when the samples are irradiated from the front side. In Figure 5b the results of identical measurements performed with excitation from the sample back side are shown. Changing from front to back side illumination reverses the **k** vector of the laser light with respect to the spin quantization axis. Because the sense of the circular polarization is defined with respect to the **k** vector of the light, changing the illumination direction interchanges cw and ccw polarization relative to the space-fixed spin quantization axis. Consequently, upon excitation from the back side, the gold substrates emit

https://doi.org/10.1021/acsnano.2c02709
ACS Nano 2022, 16, 12145−12155

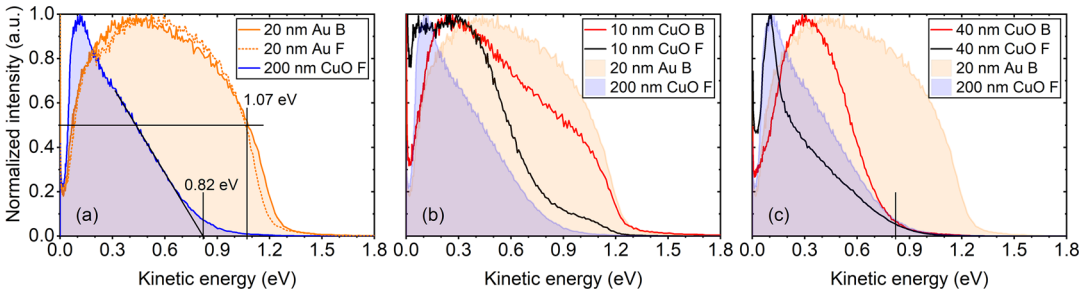

Figure 6. UV photoelectron spectra, acquired with the laser irradiating the samples at λ = 213 nm either from the front (labeled "F") or back (labeled "B") side. Shown are (a) reference spectra from a from a 200 nm thick CuO layer and the bare gold substrate and spectra from samples with (b) 10 nm and (c) 40 nm thick CuO films.

electrons with the reversed average differential spin polarization, $(P_{cw} - P_{ccw}) = (-4.4 \pm 0.3)\%$. In contrast to the observations for front side illumination, the differential electron spin polarization now increases until a CuO film thickness of ~40 nm. While for front side illumination the 10 nm thick CuO film already gives rise to the same polarization value as the CuO reference, the polarization values obtained with back side illumination are distributed in a range intermediate between what is measured on the gold and the CuO references. In the case of front side illumination, the maximum polarization values are constant from 10 nm thickness on, while in the case of back side illumination they reach the maximum value only at a thickness of 40 nm. These observations support the notion that, for back side illumination of the samples, the observed photoelectrons originate predominantly from gold, albeit with a contribution from the CuO layers.

Energy Considerations. The conclusions drawn from the differential spin polarization are corroborated by time-of-flight (ToF) UPS spectra acquired with radiation at λ = 213 nm, as used for the spin analysis. These spectra provide the electron energy distribution over which the spin polarization is averaged. In Figure 6a photoelectron spectra obtained from the bare thin-film gold substrates are shown. The dashed and solid orange lines denote photoelectrons from Au via front side and back side illumination, respectively, with the latter further highlighted by the yellow area in the graph. Here, the energy distribution of the photoelectrons and the sample work function are independent of the laser excitation direction. From the position of the Fermi edge at $E_{kin} \approx 1.07$ eV, a work function of $\Phi_{Au} \approx 4.76$ eV is calculated, which, with a small deviation, matches the value of Φ_{Au} = 4.65 eV determined above by He I UPS. Also shown in Figure 6a is the spectrum measured on a 200 nm thick CuO film excited from the front side, as a blue line and blue-shaded area. At this thickness, all photoelectrons arise from the oxide layer. The maximum kinetic energy $E_{kin} = h\nu - \text{VBE} \approx 0.82$ eV indicates that the VBE is located 5.0 eV below the vacuum level, consistent with the value determined from the He I spectra (Figure 3). Because the work functions of both materials are similar, the difference in the maximum kinetic energies in the gold and oxide spectra reflects mostly the position of the VBE below the Fermi level.

Figure 6b shows spectra acquired on a sample with a 10 nm thick CuO film. The gold and CuO reference spectra shown in Figure 6a are replicated as shaded areas for comparison. On this sample, the maximum kinetic energies match well the value found on the bare gold film, but the shape of the spectra has changed. It can be described as a composite of the Au and CuO spectra in panel (a). On the basis of the VBE of the CuO layer and the work function of the pure gold film, electrons with kinetic energies in the range of E_{kin} = 0.0–0.8 eV arise from both the gold and the oxide film, while electrons with higher energies of up to E_{kin} = 1.23 eV arise solely from the gold substrate.

The front side illumination spectra exhibit pronounced secondary electron signals at low kinetic energies. (Note that the samples were neither heated nor sputtered to avoid impairing the chiral layer structure.) The secondary electron signal varies between the individual measurements, which hampers an exact quantification of the Au and CuO contributions in the spectra. However, the Au/CuO ratio in the photoelectron signal is significantly larger for back side than for front side illumination. To obtain an estimate of the electron yield from either layer, the gold reference spectrum was scaled to match the higher-energy parts of the spectra from the 10 nm thick CuO film; see section S5 in the Supporting Information. The total photoelectron signal from the gold layer is quantified by integration over these scaled gold spectra. For each illumination direction, the area underneath the scaled gold spectrum is subtracted from the area underneath the CuO/Au spectrum; the difference is assumed to correspond to the photoelectron signal from the CuO layers. The ratios of the spectral areas indicate that, for front side illumination, the electron signal from the 10 nm thick CuO layer is ~4 times higher than the signal from the gold layer. For back side illumination, the ratio is roughly reversed, that is, only one-quarter of the photoelectrons is emitted from the oxide layer.

The spin polarization measurements shown in Figure 4c demonstrate that the sign of the spin polarization becomes independent of the direction of illumination at a CuO layer thickness of 40 nm. The photoemission spectra measured on this sample are shown in Figure 6c. In contrast to the thinner films, the maximum kinetic energy for the 40 nm CuO films is as well independent of the direction of illumination and corresponds to the value found in the reference CuO spectrum. The data therefore indicate that the contribution of electrons originating in the gold layer to the signal is negligible in oxide layers with a thickness of 40 nm, or larger.

Origin of the Photoelectron Spin Polarization. The ability of chiral oxide films to spin filter electron currents was reported previously for chiral CuO[9] and, indirectly, for chiral CoO_x[10] layers, and those findings were interpreted as a manifestation of the CISS effect. This more comprehensive study of the photoelectron spectra and spin polarization measurements indicates that the observed spin polarization depends on the electron kinetic energy and the material from which the electrons originate. In agreement with the earlier

https://doi.org/10.1021/acsnano.2c02709
ACS Nano 2022, 16, 12145–12155

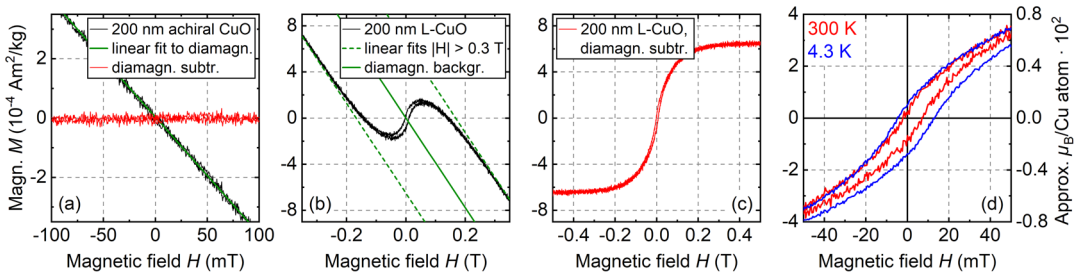

Figure 7. Magnetization curves at T = 300 K of a sample with an achiral 200 nm thick CuO film (a) and a 200 nm thick L-CuO film before (b) and after (c) subtraction of the diamagnetic substrate signal. (d) Hysteresis at T = 4.3 K (blue) and 300 K (red) on an enlarged scale.

study, the electrons arising from the gold layer underneath the oxide as well as from a finite depth in the oxide layer itself appear to be spin filtered during the transmission through the chiral oxide. As shown in Figure 4a, the spin polarization is correlated with the film chirality; this observation strongly supports the interpretation as a CISS-based phenomenon. Indeed, there is growing evidence for the occurrence of CISS in inorganic solids.[10,41−43] In addition to the spin filtering effect, however, photoelectrons generated directly from the CuO itself contribute significantly to the spin polarization, vide infra, which suggests the presence of an additional polarization mechanism in the oxide layer, distinct from the spin filtering. We elaborate on this interpretation in the following section.

The photoelectron spectra presented in Figure 6b,c can be understood as composites of the spectra of the bare gold and pure CuO. The lower-energy electrons (E_{kin} < 0.8 eV) are emitted predominantly from the CuO layer, while the higher-energy electrons (E_{kin} > 0.8 eV) originate solely from the gold. On the basis of this interpretation, the ratio of the electrons emitted from either material depends on both the oxide layer thickness and the direction of illumination. The fraction of electrons emitted from the gold layer is higher for thinner oxide layers and illumination from the back side. Figure 6c indicates that no photoelectrons from the gold layer are detected on a sample with a 40 nm thick oxide film.

As Figure 4c reveals, the sign of the spin polarization changes with the CuO film thickness and the photoexcitation geometry; this dependence correlates with the changes in the photoelectron kinetic energy distributions as a function of the photoexcitation geometry and the CuO thickness. The spin polarization is positive for back side illumination and an oxide film thickness below 40 nm. For back side illumination and thicker films as well as upon front side illumination, a negative spin polarization is found. These correlations between the data sets suggest that, for L-CuO samples, the photoelectrons originating directly from the CuO are negatively polarized, while the (higher-energy) photoelectrons originating from the Au are positively polarized. The relative numbers of photoelectrons from either layer suggests that the electrons originating from the Au exhibit a similar magnitude of polarization as those from CuO. However, the high fraction of secondary electrons in the lower-energy interval is expected to reduce the average spin polarization if the spins depolarize during the scattering events, which yield the secondary electrons. At higher energies, the relative number of secondary electrons is significantly lower, which suggests that the spin polarization in the lower-energy interval, that is, of the electrons originating predominantly in the CuO film, is initially larger than the polarization of the higher-energy electrons emitted solely from the Au film. Because linearly polarized UV light is employed, the electrons originally emitted from the Au substrate are unpolarized and must become spin polarized as they transit through the chiral structure of the CuO film. That is, they are spin filtered by the CISS effect. With respect to the Fermi level, the electrons from the CuO and Au layers have energies of 4.6−5.4 eV and up to 5.8 eV, respectively. A strong energy dependence of the spin filtering, including changes in sign on a scale of a few 100 meV, is consistent with the predictions of various model calculations,[44−47] albeit such calculations are currently only available for molecular spin-filtering systems. The correlation between the electron kinetic energy distributions and the measured average spin polarization could hence reflect the energy dependence of the CISS effect.

Apart from a CISS-related spin filtering effect, however, the measured spin polarization shows a contribution from a distinct second mechanism, where the electrons emitted from the CuO are intrinsically spin polarized. Given that the spin-polarized photoelectron distribution arises from a pure CISS-related spin filtering effect for photoelectrons originating from the Au (and inner layers of CuO) and an intrinsic spin polarization for the photoelectrons originating the CuO layer, what causes the intrinsic spin polarization in the chiral CuO? In CuO, with Cu(II), one d electron is unpaired,[48] and cupric oxide is antiferromagnetic below a Néel temperature of ∼230 K.[49] Above this temperature, the copper and oxygen atoms are thought to form one-dimensional antiferromagnetic chains in the $[10\bar{1}]$ direction.[48,50] The strength of the exchange term, which could induce long-range magnetic order, depends on the Cu−O−Cu bond angle.[49] We hypothesize that a chiral distortion of the atomic lattice could prevent the compensation of the magnetic moments of the magnetic sublattices and introduce ferrimagnetic behavior. Similarly, a Dzyaloshinsky-Moriya interaction,[20,21] arising from the asymmetrically distorted chiral CuO lattice,[25,26] may lead to a not fully compensated antiferromagnetic order.

Magnetics. To examine the magnetic properties of the chiral CuO thin films, magnetization curves were acquired with a vibrating sample magnetometer (VSM). Results of these measurements are shown in Figure 7. The $M(H)$ curves were recorded at temperatures of 4.3 and 300 K and up to maximum fields of ±9 T. A measurement at T = 300 K on a sample with an achiral 200 nm thick CuO film, shown in Figure 7a, reveals purely diamagnetic behavior, consistent with the negative susceptibility of the Au and quartz substrate materials. No deviations that would indicate the presence of a ferromagnetic contaminant are evident. In contrast, a magnetization curve measured on a sample with a chiral, 200 nm thick L-CuO layer shown in Figure 7b exhibits paramagnetic behavior and a distinct, albeit small, magnetization hysteresis, indicative of

https://doi.org/10.1021/acsnano.2c02709
ACS Nano 2022, 16, 12145−12155

ferromagnetic behavior. These signals are superimposed on the diamagnetic substrate signal. Figure 7c shows the sample curve after subtraction of the diamagnetic background (-3.9×10^{-3} $Am^2/(kgT)$) of the sample, representing only the paramagnetic signal and the ferromagnetic hysteresis of the oxide layer. From these data, a saturation magnetization of $\sim 6.3 \times 10^{-4}$ Am^2/kg at 0.5 T is determined. This value corresponds to a magnetic moment of $\sim 1.3 \times 10^{-2}$ Bohr magnetons per copper atom. Figure 7d shows a close-up view of the same data, along with corresponding data acquired at 4.3 K. The curves exhibit asymmetric zero-field magnetization values of 0.3×10^{-4} Am^2/kg and -0.9×10^{-4} Am^2/kg at 300 K and $\sim 0.6 \times 10^{-4}$ Am^2/kg and -1.6×10^{-4} Am^2/kg at 4.3 K. An average coercive field strength of ~5 mT is determined at 300 K, which increases to 9 mT at 4.3 K. Because of the ultrathin film thickness, the absolute oxide amount in the samples is low. To assign the ferromagnetic behavior to the oxide layer, a possible contamination with ferromagnetic elements was assessed through high-resolution XPS spectra acquired in the 2p peak regions of the ferromagnetic elements Cr, Mn, Fe, Co, and Ni. On the basis of these data, contamination above the XPS detection threshold of ~0.1 atom % in the probed surface layers (up to several nanometers depth) was ruled out. Subsequently, time-of-flight secondary ion mass spectra (ToF-SIMS) were acquired, probing the entire layer thickness, which did not reveal any ferromagnetic contamination either; see section S3 in the Supporting Information. Ferromagnetic behavior of transition metal oxides is discussed in the literature as a consequence of oxygen vacancies and interfacial effects.[51−58]

The finding of these hitherto rather explorative measurements is that the chiral CuO layers, in contrast to their achiral counterparts, can exhibit ferrimagnetic behavior. It supports the hypothesis that the energy dependence of the measured spin polarization reflects an interplay of CISS and a magnetization in the material rather than solely the energy dependence of the CISS effect. The origin of the magnetization of the CuO layers is not yet identified. The chiral CuO films were shown to have textures that preferentially expose chiral planes along the sample surface;[17,18,22] all chiral planes have Miller indices (hkl) with $k \neq 0$.[27] The copper atoms in the oxide form one-dimensional antiferromagnetic chains along the $[10\bar{1}]$ direction.[48,50] Since $k = 0$, this orientation cannot be exactly perpendicular to any chiral plane. We argue that the atomic lattice of the CuO films is chirally distorted, consistent with findings by Widmer et al.[22] using XPD and by Bai et al.[28,29] using a TEM analysis. The observed monotonous increase of the CD magnitude with the film thickness (Figure 2b) supports this argument. We hypothesize that the chiral, stressed lattice exhibits a canted spin order,[59] which introduces a magnetic moment with a fixed orientation within the crystal lattice that is perpendicular to the direction of the AF ordering. As mentioned above, the direction of the AF ordering is never exactly perpendicular to the preferentially exposed chiral planes. Therefore, even though the plane in which the magnetic moment induced by the spin canting lies is not known, the magnetic moment will generally have a component perpendicular to the chiral planes. Simultaneously, the film textures imply that most CuO crystallites have the same out-of-plane orientation. The spin canting-induced magnetic moments thus have nonzero components perpendicular to the sample surface, and these components do not cancel out even if the in-plane (azimuthal) orientation of the crystallites is random; see section S6 of the Supporting Information.

Testing this hypothesis will require further experimental investigations, beyond the scope of the present study. Employing energy-resolved spin polarization measurements, the contribution of the bulk CuO can be singled out when well-defined magnetizations of the samples are related to the spin polarization of emitted photoelectrons. However, the asymmetric remanent magnetization values evident in Figure 7d are consistent with a magnetization bias introduced by the proposed mechanism. A chirality-induced magnetization switching of ferromagnets, which would manifest itself similarly in a shifted zero-field magnetization, was recently observed by Paltiel and co-workers after adsorption of α-helix polyalanine on a cobalt substrate.[60,61] This effect was attributed to a charge polarization upon adsorption of the molecules that is accompanied by a spin polarization along the molecules.[62]

SUMMARY AND OUTLOOK

In conclusion, cupric oxide thin films electrodeposited on polycrystalline Au film electrodes from a solution of Cu^{2+}/tartaric acid were shown to exhibit strong circular dichroism that depends on the enantiomeric form of the tartaric acid in solution. The chiral CuO films were studied by Mott polarimetry and magnetometry. By controlling both the illumination direction and the oxide film thickness, the relative number of photoelectrons originating from the gold substrate and from the copper oxide layer could be distinguished. Analysis of the photoelectron spectra and the spin polarization measurements indicates that the spin polarization of photoelectrons emitted from the Au/CuO layer system depends on the origin of the photoelectrons. The analysis shows that the photoelectrons originating from the gold substrate are spin filtered by the chiral oxide layers, as a manifestation of the CISS effect. The energy dependence of the spin filtering is consistent with theoretical considerations of models of helical organic systems[43,46] and helical minimal models.[45] Beyond this notion, the measured spin polarization values could be rationalized as a sum of two contributions by assuming that photoelectrons emitted from the oxide layer are intrinsically spin polarized. We hypothesize that the chiral modification of the oxides lifts the antiferromagnetic compensation of the magnetic moments of the unpaired copper d electrons and introduces ferrimagnetic behavior. Indeed, a weak magnetization hysteresis was evident in VSM measurements, which could not be related to a possible ferromagnetic contamination of the samples. The definitive determination of the nature of these mechanisms will require quantitative knowledge about the energy dependence of the spin polarization, and it is a subject of future investigations.

METHODS

Film Deposition. The film deposition procedure, as adopted from Switzer et al.,[17−19] was described previously.[9] For the electrodeposition a PAR model 173 galvanostat was used. The reference and counter electrode consisted of an Ag/AgCl electrode and a Pt foil, respectively. The Au substrates acted as the working electrode. The electrodeposition solution comprised 0.2 M $CuSO_4$ (≥98.0%, EM Science) and 0.2 M L-tartaric acid (≥99.5%, Sigma-Aldrich) or D-tartaric acid (≥99.0%, Sigma-Aldrich) in 3 M NaOH. The current density controlled at the working electrode was 0.5 mA/cm^2. Depending on the desired film thickness, the deposition time was varied between 10 min and 1 h. After the deposition procedure, all samples were baked at 450 °C for 1 h to ensure the complete

https://doi.org/10.1021/acsnano.2c02709
ACS Nano 2022, 16, 12145−12155

oxidation of the films from Cu_2O to CuO and remove any organic residues.

XPS Measurements. XPS measurements were performed on a Kratos Axis Ultra system using monochromatized Al K_α radiation at $h\nu$ = 1486.6 eV. The binding energy scale was calibrated to the Fermi edge and the C 1s peak at 284.8 eV.

He(I) UPS Measurements. The He(I) UPS measurements were conducted emloying He(I) radiation at $h\nu$ = 21.22 eV and a SPECS Phoibos 150 hemispherical analyzer. Throughout the measurements, a sample bias of −4.0 V was applied.

213 nm UPS Measurements. Ultraviolet photoelectron spectra were acquired employing the same laser radiation as used for the spin polarization measurements and inside the same UHV chamber. In contrast to these measurements, the laser impinged onto the sample surface under an angle of 60° with respect to the surface normal. The electrons were detected around the surface normal. Energy resolution was achieved using a 400 mm long time-of-flight tube; the electrons were registered by a microchannel plate detector.

Absorption and CD Measurements. UV−Vis absorption measurements were performed using a Jasco V-770 absorption spectrometer at a measurement speed of 100 nm/min and with both step size and bandwidth set to 1 nm. For the optical CD measurements a Jasco J-815 CD spectrometer was used. The data were recorded at 100 nm/min and with a pitch of 0.2 nm and an integration time of 1 s. The CD specta were each averaged over three runs. In each case, the sample was mounted on a custom-designed sample holder in which the samples were oriented perpendicularly to the light direction. The sample holder included an aperture of approximately 2 × 4 mm^2, exposing only the oxide-coated surface area to the light. All optical measurements were corrected for a baseline measurement on a bare quartz/Au substrate sample.

Spin Polarization Measurements. The spin polarization of photoelectrons emitted from the samples was measured in a Mott scattering apparatus, illustrated in Figure 4a. As described previously,[9] photoelectrons are excited by laser pulses at λ = 213 nm ($h\nu$ = 5.83 eV) with a pulse duration of 200 ps and at a repetition rate of 20 kHz. The light impinges on the samples along the surface normal, perpendicular to the surface plane, and the photoelectrons are as well collected along the surface normal. Electron optics guide the electrons toward a scattering target that is set to a potential of +50 kV, accelerating the electrons to weakly relativistic energies. Two detectors placed symmetrically around the incident electron beam at angles of ±120° register electrons that are backscattered from the target. Because of the high scattering energy, the nuclei of the scattering target, which consists of a 70 nm thin gold foil, generate a magnetic field in the rest frame of the electrons and introduce a spin-dependent term into the scattering potential. The intensity asymmetry $A = (I_u - I_l)/(I_u + I_l)$ in the number of electrons I_u and I_l scattered into the upper and lower detectors, respectively, is therefore a measure of the average spin polarization of the emitted photoelectrons. The spin polarization P is connected with this asymmetry A via the analyzing power or Sherman function S of the Au scattering foil by $P = A/S$. Because the scattering cross section only depends on the projection of the spin onto the direction of the magnetic field, the electron optics include an element to bend the electron beam by 90°, converting an initially longitudinal spin polarization into a transverse polarization prior to the Mott scattering process. This means that the spin polarization along the surface normal of the samples is measured in the present configuration. Throughout the measurement procedure, the polarization of the laser light is interchanged from s-linear to clockwise and counterclockwise circular by rotation of a quarter-wave plate (QWP). At each position of the QWP, ~10^4 electrons are collected. After a full QWP rotation, the measurement position is interchanged between the sample and a polycrystalline gold substrate without an oxide layer mounted directly beneath the sample. The polycrystalline gold emits unpolarized electrons upon excitation with linearly polarized light and is used to correct for instrumental asymmetries. The measurements were conducted under ultrahigh vacuum (UHV) conditions at a base pressure of less than 3 × 10^{-9} Torr. The UHV chamber comprised a permalloy shielding against external magnetic fields and was placed inside three Helmholtz coils, which compensate for the earth's magnetic field. The residual magnetic fields are smaller than ~20 μT.

VSM Measurements. The magnetization curves were recorded using the vibrating sample magnetometry option of a Quantum Design DynaCool physical property measurement system (PPMS). The $M(H)$ curves were recorded at temperatures of 4.3 and 300 K and up to maximum fields of ±9 T. The entire samples were probed. The samples were mounted longitudinally using the original Quantum Design sample holders; that is, the in-plane component was measured.

ASSOCIATED CONTENT

Supporting Information

The Supporting Information is available free of charge at https://pubs.acs.org/doi/10.1021/acsnano.2c02709.

Additional XPS spectra, ToF-SIMS data, topographic AFM images, optical absorption data, information on the electron yield from the Au and CuO layers, and an illustration of the spin-canted magnetic order within the oxide layers (PDF)

AUTHOR INFORMATION

Corresponding Authors

Paul V. Möllers − *Department of Physics and Center for Soft Nanoscience (SoN), Westfälische Wilhelms-Universität Münster, 48149 Münster, Germany;* orcid.org/0000-0002-6916-7664; Email: paul.moellers@uni-muenster.de

Helmut Zacharias − *Department of Physics and Center for Soft Nanoscience (SoN), Westfälische Wilhelms-Universität Münster, 48149 Münster, Germany;* orcid.org/0000-0001-9807-1103; Email: hzach@uni-muenster.de

Authors

Jimeng Wei − *Chemistry Department, University of Pittsburgh, 15260 Pittsburgh, Pennsylvania, United States*

Soma Salamon − *Faculty of Physics and Center for Nanointegration Duisburg-Essen (CENIDE), Universität Duisburg-Essen, 47057 Duisburg, Germany;* orcid.org/0000-0002-8661-6038

Manfred Bartsch − *Department of Physics and Center for Soft Nanoscience (SoN), Westfälische Wilhelms-Universität Münster, 48149 Münster, Germany*

Heiko Wende − *Faculty of Physics and Center for Nanointegration Duisburg-Essen (CENIDE), Universität Duisburg-Essen, 47057 Duisburg, Germany;* orcid.org/0000-0001-8395-3541

David H. Waldeck − *Chemistry Department, University of Pittsburgh, 15260 Pittsburgh, Pennsylvania, United States;* orcid.org/0000-0003-2982-0929

Complete contact information is available at: https://pubs.acs.org/10.1021/acsnano.2c02709

Notes

The authors declare no competing financial interest.

ACKNOWLEDGMENTS

We gratefully thank Dr. B. Tyler from the Münster Nanofabrication Facility for taking the ToF-SIMS spectra, and we thank Dr. B. P. Bloom for helpful discussions. Partial financial support through the Volkswagen Stiftung (H.Z., Grant No. 96451) and the NSF−DFG project "Echem: Spin-polarized electrons for spin selective electrocatalysis", Grant No. Za 110/30-1 (H.Z.), and by the United States National

Science Foundation (NSF) through CHE-1900078 and CHE-2140249 (D.H.W.) is gratefully acknowledged. Partial financial support by the German Research Foundation (DFG) via the CRC/TRR 247 (ID 388390466, Project B02) (H.W.) is gratefully acknowledged.

REFERENCES

(1) Fujishima, A.; Honda, K. Electrochemical Photolysis of Water at a Semiconductor Electrode. *Nature* **1972**, *238*, 37−38.
(2) Grätzel, M. Photoelectrochemical Cells. *Nature* **2001**, *414*, 338−344.
(3) Hisatomi, T.; Kubota, J.; Domen, K. Recent Advances in Semiconductors for Photocatalytic and Photoelectrochemical Water Splitting. *Chem. Soc. Rev.* **2014**, *43*, 7520−7535.
(4) Voiry, D.; Shin, H. S.; Loh, K. P.; Chhowalla, M. Low-Dimensional Catalysts for Hydrogen Evolution and CO_2 Reduction. *Nat. Rev. Chem.* **2018**, *2*, 105.
(5) Dau, H.; Limberg, C.; Reier, T.; Risch, M.; Roggan, S.; Strasser, P. The Mechanism of Water Oxidation: From Electrolysis Via Homogeneous to Biological Catalysis. *Chem. Catal. Chem.* **2010**, *2*, 724−761.
(6) Mtangi, W.; Kiran, V.; Fontanesi, C.; Naaman, R. Role of the Electron Spin Polarization in Water Splitting. *J. Phys. Chem. Lett.* **2015**, *6*, 4916−4922.
(7) Mtangi, W.; Tassinari, F.; Vankayala, K.; Vargas Jentzsch, A.; Adelizzi, B.; Palmans, A. R. A.; Fontanesi, C.; Meijer, E. W.; Naaman, R. Control of Electrons' Spin Eliminates Hydrogen Peroxide Formation During Water Splitting. *J. Am. Chem. Soc.* **2017**, *139*, 2794−2798.
(8) Zhang, W.; Banerjee-Ghosh, K.; Tassinari, F.; Naaman, R. Enhanced Electrochemical Water Splitting with Chiral Molecule-Coated Fe_3O_4 Nanoparticles. *ACS Energy Lett.* **2018**, *3*, 2308−2313.
(9) Ghosh, K. B.; Zhang, W.; Tassinari, F.; Mastai, Y.; Lidor-Shalev, O.; Naaman, R.; Möllers, P.; Nürenberg, D.; Zacharias, H.; Wei, J.; Wierzbinski, E.; Waldeck, D. H. Controlling Chemical Selectivity in Electrocatalysis with Chiral CuO-Coated Electrodes. *J. Phys. Chem. C* **2019**, *123*, 3024−3031.
(10) Ghosh, S.; Bloom, B. P.; Lu, Y.; Lamont, D.; Waldeck, D. H. Increasing the Efficiency of Water Splitting Through Spin Polarization Using Cobalt Oxide Thin Film Catalysts. *J. Phys. Chem. C* **2020**, *124*, 22610−22618.
(11) Naaman, R.; Paltiel, Y.; Waldeck, D. H. Chiral Molecules and the Electron Spin. *Nat. Rev. Chem.* **2019**, *3*, 250−260.
(12) Göhler, B.; Hamelbeck, V.; Markus, T. Z.; Kettner, M.; Hanne, G. F.; Vager, Z.; Naaman, R.; Zacharias, H. Spin Selectivity in Electron Transmission Through Self-Assembled Monolayers of Double-Stranded DNA. *Science* **2011**, *331*, 894−897.
(13) Kettner, M.; Bhowmick, D. K.; Bartsch, M.; Göhler, B.; Zacharias, H. A Silicon-Based Room Temperature Spin Source without Magnetic Layers. *Adv. Mater. Interfaces* **2016**, *3*, 1600595.
(14) Möllers, P. V.; Ulku, S.; Jayarathna, D.; Tassinari, F.; Nürenberg, D.; Naaman, R.; Achim, C.; Zacharias, H. Spin-Selective Electron Transmission Through Self-Assembled Monolayers of Double-Stranded Peptide Nucleic Acid. *Chirality* **2021**, *33*, 93−102.
(15) Kettner, M.; Göhler, B.; Zacharias, H.; Mishra, D.; Kiran, V.; Naaman, R.; Fontanesi, C.; Waldeck, D. H.; Sęk, S.; Pawlowski, J.; Juhaniewicz, J. Spin Filtering in Electron Transport Through Chiral Oligopeptides. *J. Phys. Chem. C* **2015**, *119*, 14542−14547.
(16) Kettner, M.; Maslyuk, V. V.; Nürenberg, D.; Seibel, J.; Gutierrez, R.; Cuniberti, G.; Ernst, K. H.; Zacharias, H. Chirality-Dependent Electron Spin Filtering by Molecular Monolayers of Helicenes. *J. Phys. Chem. Lett.* **2018**, *9*, 2025−2030.
(17) Switzer, J. A.; Kothari, H. M.; Poizot, P.; Nakanishi, S.; Bohannan, E. W. Enantiospecific Electrodeposition of a Chiral catalyst. *Nature* **2003**, *425*, 490−493.
(18) Kothari, H. M.; Kulp, E. A.; Boonsalee, S.; Nikiforov, M. P.; Bohannan, E. W.; Poizot, P.; Nakanishi, S.; Switzer, J. A. Enantiospecific Electro-Deposition of Chiral CuO Films from Copper(II) Complexes of Tartaric and Amino Acids on Single-Crystal Au(001). *Chem. Mater.* **2004**, *16*, 4232−4244.
(19) Poizot, P.; Hung, C. J.; Nikiforov, M. P.; Bohannan, E. W.; Switzer, J. A. An Electrochemical Method for CuO Thin Film Deposition from Aqueous Solution. *Electrochem. Solid-State Lett.* **2003**, *6*, C21−C25.
(20) Dzyaloshinsky, I. A Thermodynamic Theory of "Weak" Ferromagnetism of Antiferromagnetics. *J. Phys. Chem. Solids* **1958**, *4*, 241−255.
(21) Moriya, T. Anisotropic Superexchange Interaction and Weak Ferromagnetism. *Phys. Rev.* **1960**, *120*, 91−98.
(22) Widmer, R.; Haug, F. J.; Ruffieux, P.; Gröning, O.; Bielmann, M.; Gröning, P.; Fasel, R. Surface Chirality of CuO Thin Films. *J. Am. Chem. Soc.* **2006**, *128* (43), 14103−14108.
(23) Tahir, D.; Tougaard, S. Electronic and Optical Properties of Cu, CuO and Cu_2O Studied by Electron Spectroscopy. *J. Phys.: Condens. Matter* **2012**, *24*, 175002.
(24) Pauly, N.; Tougaard, S.; Yubero, F. Determination of the Cu 2p Primary Excitation Spectra for Cu, Cu_2O and CuO. *Surf. Sci.* **2014**, *620*, 17−22.
(25) Gellman, A. J. Chiral Surfaces: Accomplishments and Challenges. *ACS Nano* **2010**, *4*, 5−10.
(26) Chen, Q.; Richardson, N. V. Physical Studies of Chiral Surfaces. *Annu. Rep. Prog. Chem. C* **2004**, *100*, 313−347.
(27) Bohannan, E. W.; Nicic, I. M.; Kothari, H. M.; Switzer, J. A. Enantiospecific Electrodeposition of Chiral CuO Films on Cu(110) from Aqueous Cu(II) Tartrate and Amino Acid Complexes. *Electrochim. Acta* **2007**, *53*, 155−160.
(28) Bai, T.; Ai, J.; Liao, L.; Luo, J.; Song, C.; Duan, Y.; Han, L.; Che, S. Chiral Mesostructured NiO Films with Spin Polarisation. *Angew. Chem., Int. Ed.* **2021**, *60*, 9421−9426.
(29) Bai, T.; Ai, J.; Duan, Y.; Han, L.; Che, S. Spin Selectivity of Chiral Mesostructured Iron Oxides with Different Magnetisms. *Small* **2022**, *18*, 2104509.
(30) Ghijsen, J.; Tjeng, L. H.; van Elp, J.; Eskes, H.; Westerink, J.; Sawatzky, G. A.; Czyzyk, M. T. Electronic Structure of Cu_2O and CuO. *Phys. Rev. B* **1988**, *38*, 11322−11330.
(31) Ching, W. Y.; Xu, Y. N.; Wong, K. W. Ground-State and Optical Properties of Cu_2O and CuO Crystals. *Phys. Rev. B* **1989**, *40*, 7684−7695.
(32) Morasch, J.; Wardenga, H. F.; Jaegermann, W.; Klein, A. Influence of Grain Boundaries and Interfaces on the Electronic Structure of Polycrystalline CuO Thin Films. *Phys. Status Solidi A* **2016**, *213*, 1615−1624.
(33) Benndorf, C.; Caus, H.; Egert, B.; Seidel, H.; Thieme, F. Identification of Cu(I) and Cu(II) Oxides by Electron Spectroscopic Methods: AES, ELS and UPS Investigations. *J. Electron Spectrosc. Relat. Phenom.* **1980**, *19*, 77−90.
(34) Scudiero, L.; Barlow, D. E.; Mazur, U.; Hipps, K. W. Scanning Tunneling Microscopy, Orbital-Mediated Tunneling Spectroscopy, and Ultraviolet Photoelectron Spectroscopy of Metal(II) Tetraphenylporphyrins Deposited from Vapor. *J. Am. Chem. Soc.* **2001**, *123*, 4073−4080.
(35) Wu, D.; Zhang, Q.; Tao, M. LSDA+U Study of Cupric Oxide: Electronic Structure and Native Point Defects. *Phys. Rev. B* **2006**, *73*, 235206.
(36) Koffyberg, F. P.; Benko, F. A. A Photoelectrochemical Determination of the Position of the Conduction and Valence Band Edges of p-Type CuO. *J. Appl. Phys.* **1982**, *53*, 1173−1177.
(37) Seah, M. P.; Dench, W. A. Quantitative Electron Spectroscopy of Surfaces: A Standard Data Base for Electron Inelastic Mean Free Paths in Solids. *Surf. Interface Anal.* **1979**, *1*, 2−11.
(38) Borstel, G.; Wöhlecke, M. Spin Polarization of Photoelectrons Emitted from Nonmagnetic Solids. *Phys. Rev. B* **1982**, *26*, 1148−1155.
(39) Wöhlecke, M.; Borstel, G. On the Role of Spin-Orbit Coupling and Crystal Symmetry on the Spin-Polarization of Photoelectrons in Nonmagnetic Crystals. *Phys. Scr.* **1983**, *T4*, 162−164.
(40) Vasilyev, D.; Medjanik, K.; Babenkov, S.; Ellguth, M.; Schönhense, G.; Elmers, H.-J. Relation between Spin-Orbit Induced

https://doi.org/10.1021/acsnano.2c02709
ACS Nano 2022, 16, 12145−12155

Spin Polarization, Fano-Effect and Circular Dichroism in Soft X-Ray Photoemission. *J. Phys.: Condens. Matter* **2020**, *32*, 135501.
(41) Inui, A.; Aoki, R.; Nishiue, Y.; Shiota, K.; Kousaka, Y.; Shishido, H.; Hirobe, D.; Suda, M.; Ohe, J.; Kishine, J.; Yamamoto, H. M.; Togawa, Y. Chirality-Induced Spin-Polarized State of a Chiral Crystal $CrNb_3S_6$. *Phys. Rev. Lett.* **2020**, *124*, 166602.
(42) Nabei, Y.; Hirobe, D.; Shimamoto, Y.; Shiota, K.; Inui, A.; Kousaka, Y.; Togawa, Y.; Yamamoto, H. M. Current-Induced Bulk Magnetization of a Chiral Crystal $CrNb_3S_6$. *Appl. Phys. Lett.* **2020**, *117*, 052408.
(43) Shiota, K.; Inui, A.; Hosaka, Y.; Amano, R.; Ōnuki, Y.; Hedo, M.; Nakama, T.; Hirobe, D.; Ohe, J.; Kishine, J.; Yamamoto, H. M.; Shishido, H.; Togawa, Y. Chirality-Induced Spin Polarization over Macroscopic Distances in Chiral Disilicide Crystals. *Phys. Rev. Lett.* **2021**, *127*, 126602.
(44) Gutierrez, R.; Díaz, E.; Gaul, C.; Brumme, T.; Domínguez-Adame, F.; Cuniberti, G. Modeling Spin Transport in Helical Fields: Derivation of an Effective Low-Dimensional Hamiltonian. *J. Phys. Chem. C* **2013**, *117*, 22276−22284.
(45) Michaeli, K.; Naaman, R. Origin of Spin-Dependent Tunneling Through Chiral Molecules. *J. Phys. Chem. C* **2019**, *123*, 17043−17048.
(46) Geyer, M.; Gutierrez, R.; Cuniberti, G. Effective Hamiltonian Model for Helically Constrained Quantum Systems within Adiabatic Perturbation Theory: Application to the Chirality-Induced Spin Selectivity (CISS) Effect. *J. Chem. Phys.* **2020**, *152*, 214105.
(47) Liu, Y.; Xiao, J.; Koo, J.; Yan, B. Chirality-Driven Topological Electronic Structure of DNA-like Materials. *Nat. Mater.* **2021**, *20*, 638−644.
(48) Filippetti, A.; Fiorentini, V. Magnetic Ordering in CuO from First Principles: A Cuprate Antiferromagnet with Fully Three-Dimensional Exchange Interactions. *Phys. Rev. Lett.* **2005**, *95*, 086405.
(49) Yang, B. X.; Thurston, T. R.; Tranquada, J. M.; Shirane, G. Magnetic Neutron Scattering Study of Single-Crystal Cupric Oxide. *Phys. Rev. B* **1989**, *39*, 4343−4349.
(50) Koo, H. J.; Whangbo, M. H. Magnetic Superstructures of Cupric Oxide CuO as Ordered Arrangements of One-Dimensional Antiferromagnetic Chains. *Inorg. Chem.* **2003**, *42*, 1187−1192.
(51) Sundaresan, A.; Bhargavi, R.; Rangarajan, N.; Siddesh, U.; Rao, C. N. R. Ferromagnetism as a Universal Feature of Nanoparticles of the Otherwise Nonmagnetic Oxides. *Phys. Rev. B* **2006**, *74*, 161306.
(52) Rehman, S.; Mumtaz, A.; Hasanain, S. K. Size Effects on the Magnetic and Optical Properties of CuO Nanoparticles. *J. Nanopart. Res.* **2011**, *13*, 2497−2507.
(53) Punnoose, A.; Magnone, H.; Seehra, M. S.; Bonevich, J. Bulk to Nanoscale Magnetism and Exchange Bias in CuO Nanoparticles. *Phys. Rev. B* **2001**, *64*, 174420.
(54) Mishra, S. R.; Losby, J.; Dubenko, I.; Roy, S.; Ali, N.; Marasinghe, K. Magnetic Properties of Mechanically Milled Nano-sized Cupric Oxide. *J. Magn. Magn. Mater.* **2004**, *279*, 111−117.
(55) Osorio-Guillén, J.; Lany, S.; Barabash, S. V.; Zunger, A. Nonstoichiometry as a Source of Magnetism in Otherwise Non-magnetic Oxides: Magnetically Interacting Cation Vacancies and Their Percolation. *Phys. Rev. B* **2007**, *75*, 184421.
(56) Hou, X.; Liu, H.; Sun, H.; Liu, L.; Jia, X. Significant Room-Temperature Ferromagnetism in Porous ZnO Films: The Role of Oxygen Vacancies. *Mater. Sci. Eng., B* **2015**, *200*, 22−27.
(57) Xie, J.; Cheng, B.; Liu, L.; Liu, W.; Ren, S.; Miao, T.; Gao, C.; Zhou, G.; Qin, H.; Hu, J. The Mechanism of Photo-Regulated Magnetization in Copper Oxide Films on Pt Substrate. *Solid State Commun.* **2019**, *303*−*304*, 113732.
(58) Arbuzova, T. I.; Naumov, S. V.; Arbuzov, V. L.; Druzhkov, A. P. Anomalous Magnetic Properties of Electron-Irradiated Antiferromagnetic Copper Monoxide. *Phys. Solid State* **2009**, *51*, 953−960.
(59) Dmitrienko, V. E.; Ovchinnikova, E. N.; Collins, S. P.; Nisbet, G.; Beutier, G.; Kvashnin, Y. O.; Mazurenko, V. V.; Lichtenstein, A. I.; Katsnelson, M. I. Measuring the Dzyaloshinskii-Moriya Interaction in a Weak Ferromagnet. *Nat. Phys.* **2014**, *10*, 202−206.
(60) Ben Dor, O.; Yochelis, S.; Radko, A.; Vankayala, K.; Capua, E.; Capua, A.; Yang, S.-H.; Baczewski, L. T.; Parkin, S. S. P.; Naaman, R.; Paltiel, Y. Magnetization Switching in Ferromagnets by Adsorbed Chiral Molecules Without Current or External Magnetic Field. *Nat. Commun.* **2017**, *8*, 14567.
(61) Meirzada, I.; Sukenik, N.; Haim, G.; Yochelis, S.; Baczewski, L. T.; Paltiel, Y.; Bar-Gill, N. Long-Time-Scale Magnetization Ordering Induced by an Adsorbed Chiral Monolayer on Ferromagnets. *ACS Nano* **2021**, *15*, 5574−5579.
(62) Naaman, R.; Paltiel, Y.; Waldeck, D. H. Chiral Molecules and the Spin Selectivity Effect. *J. Phys. Chem. Lett.* **2020**, *11*, 3660−3666.

https://doi.org/10.1021/acsnano.2c02709
ACS Nano 2022, 16, 12145−12155